



Dual-angle open field wavefront sensor for simultaneous measurements of the central and peripheral human eye

DMITRY ROMASHCHENKO^{1,*}  AND LINDA LUNDSTRÖM¹ 

¹*Department of Applied Physics, Royal Institute of Technology, Stockholm, 11421, Sweden*

*dmitry.romashchenko@biox.kth.se

<https://www.aphys.kth.se/biox/research/vio>

Abstract: We have developed a novel dual-angle open field wavefront sensor. This device captures real-time foveal and peripheral Zernike aberrations, while providing natural binocular viewing conditions for the subjects. The simultaneous data recording enables accurate analysis of changes in ocular optics with accommodation overcoming any uncertainties caused by accommodative lag or lead. The instrument will be used in myopia research to study central and peripheral ocular optics during near work and to investigate the effects of optical myopia control interventions. Proof of concept measurements, performed on an artificial eye model and on 3 volunteers, showed good repeatability with foveal-peripheral data synchronization of 65 msec or better. The deviations from subjective cycloplegic refractions were not more than 0.31 D. Furthermore, we tested the dual-angle wavefront sensor in two novel measurement schemes: (1) focusing on a close target, and (2) accommodation step change.

© 2020 Optical Society of America under the terms of the [OSA Open Access Publishing Agreement](#)

1. Introduction

Investigation of the peripheral optical errors is of interest in vision science for several reasons. First of all, sufficient quality of the image on the peripheral retina is essential for many everyday activities that utilize high contrast detection and low contrast resolution. These include driving [1–3], mobility [4,5], and search tasks [6]. Additionally, it has been shown that there is a link between the peripheral retinal image and myopia [7]. The retinal image, in its turn, is mainly defined by the optical properties of the cornea and the crystalline lens. Thus, during the process of accommodation, when the shape of the crystalline lens changes, the properties of the peripheral retinal image also change [8–12]. Therefore, a device that simultaneously measures peripheral optics and accommodation state of the eye provides a more comprehensive description of the eye's optical system.

The connection between accommodation, retinal image and myopia development is not fully revealed yet. Myopia has been recognized as a global problem several years ago [7]. But its prevalence is still increasing [7,13–15], and the exact mechanisms behind its onset and development are not completely understood yet [13,16–18]. Several authors have reported that prolonged indoor activities, associated with near work and accommodation, can be considered myopia development risk factors [18–22]. However, attempts to prevent myopia with near-addition spectacles were inefficient, which proved that the possible link between myopia and accommodation is not straight-forward. Studies in guinea pigs [23], monkeys [24–27] and chickens [28,29] have shown that myopia development can also be driven by inducing defocus either in the foveal or peripheral retinal image. This became the base for developing optical myopia control interventions; currently the most effective of those are multifocal contact lenses, multifocal spectacles, and orthokeratology [30,31]. Also, the recently developed D.I.M.S. spectacles have been reported to be efficient for reducing myopia progression [32]. Even so, the effect of all these treatments is still limited and subject-dependent [30–32]. To be able to improve

the treatment effect we need a more detailed understanding of the image formed on the retina, particularly under different accommodation demands. This is also supported by previous works showing that the efficient optical myopia control interventions do not only shift the location of the peripheral image, but also have considerable effect on the peripheral image as a whole [30,31,33,34].

The amount of available data on peripheral ocular optics of an accommodating eye is currently rather small. A few previous studies report peripheral optical quality with accommodation [10,11] while the majority of the previous work focus only on peripheral refractive errors for different states of accommodation [8,9,12,35–37]. The studies of the peripheral optical quality are limited to very few accommodation steps (1 excluding the far-away target). The studies of the peripheral refractive errors, even though very thorough, do not agree on the effect of accommodation on the relative peripheral refraction (RPR). The results for both myopes and emmetropes during accommodation vary between myopic shift in RPR [8,10,12], no change in RPR [10,11,35–37], and hypermetropic shift in RPR [9]. Note that the actual accommodation state of the eye was not monitored in any of these experiments (including the peripheral optical quality works). The varying results might therefore be a consequence of accommodative lag, which is subject-dependent and difficult to predict beforehand.

The human eye is a dynamic optical system, and time-dependent fluctuations have to be considered to fully describe this system. Even when fixating on an object, the eye undergoes fluctuations both in gaze direction (microsaccades, drift and tremor) and in its optical characteristics. The dynamics of these optical characteristics in the fovea are known as accommodation microfluctuations, and their magnitude is highly dependent on the accommodation state of the eye [38]. Previous studies of accommodation microfluctuations have shown that myopes tend to have higher magnitude of the microfluctuations compared to emmetropes [39–43]. However, to the best of our knowledge, there are no publications analysing the effect of accommodation microfluctuations on peripheral vision for either relaxed or accommodating eye. Thus, the question whether they have any noticeable effect on the peripheral retinal image remains unanswered. Furthermore, knowing the possible role of peripheral retinal image in myopia development, the comparison of peripheral microfluctuations between myopic and emmetropic subjects can be a valuable contribution to overall understanding of myopia onset and progression mechanisms.

Therefore, in an attempt to reduce these knowledge gaps, we have developed a novel dual-angle open field wavefront sensor. The system consists of two measurements channels, each with a Hartmann-Shack wavefront sensor, providing simultaneous foveal and peripheral measurements. In order to analyse the behavior of the ocular optics, the wavefront data is recorded in real-time. The natural viewing conditions, provided by the open field of view, allow to design experiments in close-to-real-life settings. Potential applications of such a device are rather broad and span from basic investigations of the optical properties of the human eye to comparisons of specific myopia control interventions.

2. Design of the device

The main features of the dual-angle open field wavefront sensor are listed below:

- Open field of view provides natural viewing condition. For an emmetropic subject, the field of view is 50° horizontally and 60° vertically through the hot mirror.
- Simultaneous measurements at two horizontal visual field (VF) angles of the same eye. The separation angle can be manually adjusted in the interval between 15° and 30°. The chosen angle value is constant during the experiment (for this article, the separation angle was fixed at 20°).
- Maximum accepted pupil diameter 9 mm (restricted by the sensor size).

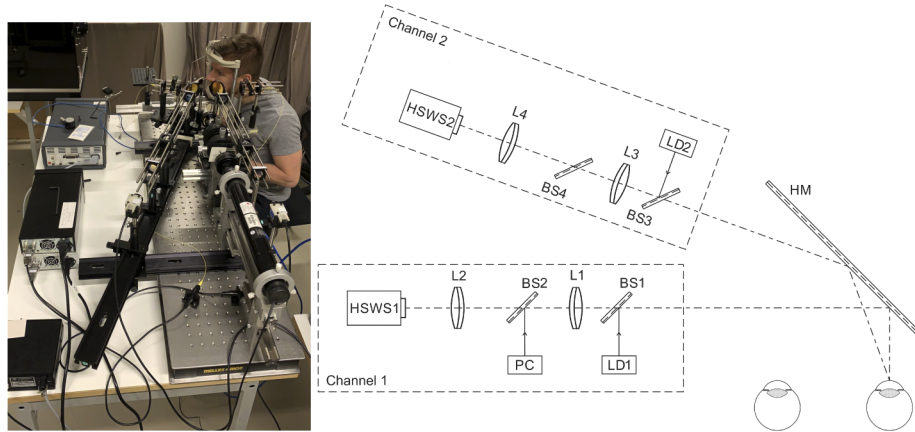
- Theoretical limits for ametropia measurements are ± 5.00 D for a 7.5 mm pupil diameter (restricted by the setup).
- Induced accommodation demands of up to 5.00 D.
- The device allows to perform measurements either on the left or right eye of a subject.
- Real-time measurements with an average sampling rate 7.5 ± 0.5 Hz.
- Average synchronization error between the two measurement channels is estimated to 65 msec (half-time of one frame acquisition at 7.5 Hz).
- Custom-developed processing routine (capable of identifying most of the blinks, corneal reflections, and track rapid gaze direction changes) enables the usage of a wide variety of focusing targets, both static and dynamic.

2.1. Optical setup

Figure 1 shows a photo and a schematic drawing of the developed device. The system includes two measurement channels aligned to the same object plane, but separated by 20° , to facilitate simultaneous central and peripheral data acquisition on the same eye. Each of these channels consists of the following principal components:

- A *2-lens telescope* (L1 + L2; L3 + L4) creates a demagnified (magnification = 0.5) projection of the entrance pupil of the eye onto the lenslet array of the wavefront sensors. In order to minimize the noise from scattering within the ocular media, each of the telescopes have an additional diaphragm located at the back focal plane of the Badal lenses (lenses L1 and L3 respectively). This diaphragm, however, also restricts the extent of ametropia that can be studied without cutting the edges of the measured wavefront. In the current configuration the limits are ± 5.00 D for a 7.5 mm pupil diameter.
- *Pellicle beam splitters* BS2 and BS4 allow the mounting of a pupil camera (PC) in either of the measurement channels. In the current setup the pupil camera is fixed in Channel 1.
- *Laser diode light delivery systems* consist of laser diodes (LD1 and LD2; $\lambda = 830$ nm), collimators (not shown), and pellicle beam splitters (BS1 and BS3). The size of these beam splitters is chosen so that they would not be limiting the field of view of the system (2'' in diameter; all other optical components are 1'' in diameter). The output power of the laser diodes is controlled by the diode drivers (Thorlabs, Inc; not shown on the figure). The diode drivers are also incorporated with a hardware-adjustable upper limit for the diode driving current. This hardware limit is set for the power level 10 times lower than that in the standard of the Swedish Work Environment Authority (Arbetsmiljöverket [44]): $70 \mu\text{W}$ for each laser diode. The hardware limit of $70 \mu\text{W}$ per laser diode corresponds to the maximum permissible continuous wave laser exposure during 8 hours ($4.45 \cdot 10^4$ sec) in the ANSI 136.1-2000 [45]. The typical operation power is in the range 30-35 μW for each diode.

Lastly, the system includes a head-chin rest (not shown in the figure) for stabilization of the subjects, and a hot-mirror (HM) that provides open field of view for the subjects. The residual aberrations of the optical systems were compensated by calibrating each channel of the setup with a flat wavefront.



Component	Description	Manufacturer/distributor
L1, L3	Achromatic cemented doublet, 1" diameter, $f' = 300$ mm.	Thorlabs, Inc.
L2, L4	Achromatic cemented doublet, 1" diameter, $f' = 150$ mm.	
BS1, BS3	Pellicle beam splitter, 2" diameter, R:T = 45:55.	
BS2, BS4	Pellicle cube mounted beam splitter, 1" diameter, R:T = 8:92.	
LD1, LD2	Fiber-coupled laser diode, $\lambda = 830$ nm.	Edmund Optics, Inc; FLIR Systems, Inc.
HSWS1, HSWS2	Hartmann-Shack wavefront sensor, WFS30-5C.	
PC	Pupil camera (BFLY-U3-13S2M-CS + 50 mm C Series Lens).	Edmund Optics, Inc. Edmund Optics, Inc.
HM	Hot mirror, 101.6 x 127 mm; Transmission: > 85% for $\lambda = 425 - 675$ nm; Reflection: > 90% for $\lambda = 750 - 1125$ nm.	

Fig. 1. Schematic drawing of the designed dual-angle wavefront sensor. Abbreviations: PC - pupil camera; LD - laser diode; L - lens; BS - beam splitter; HM - hot mirror; HSWS - Hartmann-Shack wavefront sensor.

2.2. Data post-processing

The implemented data post processing includes recalculation of Zernike coefficients from 830 nm to 550 nm wavelength, and a custom-developed filtering algorithm. The wavelength recalculation is done according to the work of Salmon et al. [46] using ocular dispersion model by Thibos et al. [47]. For subsequent analysis of the temporal behavior of Zernike coefficients, the coefficients are scaled to the same pupil size (equal to or less than the measured one). It is also worth mentioning that peripheral Zernike coefficients are given for a circular area, inscribed in the ellipse of the peripheral pupil. The refractive errors, both for the filtering and subsequent data analysis, are calculated using 2nd, 4th and 6th order Zernike coefficients according to the following formulas:

$$\begin{aligned}
 \text{Mean Sphere}[D] &= \frac{-4\sqrt{3}c_2^0}{\text{radius}_{\text{pupil}}^2} + \frac{12\sqrt{5}c_4^0}{\text{radius}_{\text{pupil}}^2} - \frac{24\sqrt{7}c_6^0}{\text{radius}_{\text{pupil}}^2}, \\
 J_0[D] &= \frac{-2\sqrt{6}c_2^2}{\text{radius}_{\text{pupil}}^2} + \frac{6\sqrt{10}c_4^2}{\text{radius}_{\text{pupil}}^2} - \frac{12\sqrt{14}c_6^2}{\text{radius}_{\text{pupil}}^2}, \\
 J_{45}[D] &= \frac{-2\sqrt{6}c_2^{-2}}{\text{radius}_{\text{pupil}}^2} + \frac{6\sqrt{10}c_4^{-2}}{\text{radius}_{\text{pupil}}^2} - \frac{12\sqrt{14}c_6^{-2}}{\text{radius}_{\text{pupil}}^2},
 \end{aligned} \tag{1}$$

where pupil radius is in mm and Zernike coefficients are in μm .

In order to eliminate measurement artifacts from blinks and corneal reflections, we developed a custom post-processing routine. The main purpose of this filtering algorithm is not only to find the measurement artifacts, but also to avoid smoothing down of the real data fluctuations. In order to achieve this, the algorithm finds individual data points containing artifacts, removes them, and then fills the gaps using linear interpolation through the neighboring data. Thus, the main challenge is the classification of individual data points. In this routine it is done by comparing the measurements to well-known features of accommodation behavior. These include Zernike coefficients as a whole, pupil size, and gaze direction. The raw data is assessed in three steps:

1. Taking away rough artifacts.

- (a) The values of mean sphere and pupil diameter are compared to the physically possible boundaries. The pupil diameter should be between 1 mm and 9 mm, and refractive state — between +5.00 D and -10.00 D.
- (b) A sudden downward spike in the pupil diameter of more than 0.75 mm, while the neighboring measurements just before and after the spike differ by less than 0.2 mm, is classified as a blink.
- (c) A jump in any Zernike coefficient (excluding piston and tilts) of more than 3 μm occurring during one time step (for 7.5 Hz acquisition frequency one time-step corresponds to 0.13 sec) is assumed to be a measurement artifact irrespective of the pupil diameter size.
- (d) A data point for which all Zernike coefficients are zero is also classified as a measurement artifact.

2. Fine-filtering routine. This part is based on an assumption that most of the artifacts occur at high temporal frequencies whereas the valuable data is concentrated at lower temporal frequencies. Thus, if we compare the real data to its low-pass filtered copy, the artifacts would appear as a large difference between these data sets. In the suggested routine, the low-pass filtering is implemented by convolving the raw data with a uniform-height window function. Each filtered data point is calculated as:

$$y_n = \frac{1}{5}(x_{n-2} + x_{n-1} + x_n + x_{n+1} + x_{n+2}) \quad (2)$$

where x denotes the raw data points, y denotes the filtered data points, and n is the index of the raw and filtered data points. The thresholds for classifying the difference between the raw and the low-pass filtered data as an artifact are:

- (a) Pupil diameter difference of more than 1 mm (considered a blink).
- (b) Mean sphere difference of more than 3.00 D.

3. Additional information extraction. The real-time spotfield image location, provided by the wavefront sensors, can be used to extract additional information about the eye's decentration and rotation dynamics. As shown in the supplementary material, if an eye would change the gaze direction when keeping the lateral position unchanged, it would correspond to a decentration of the spotfield image on the Hartmann-Shack wavefront sensor (see Appendix 1, Fig. 5). If we then make a comparison between the raw and the low-pass filtered data (analogous to the 'Fine-filtering routine'), we can investigate the stability of target fixation for the measured subject (for example during reading). In this case the 'fixation instability' will include both ocular rotation and lateral movements. If the lateral position of a subject is stabilized by a bite bar, the observed fixation deviations, decentring the spotfield image, will be mainly originating from gaze direction changes.

Once the artifacts are identified, the corresponding measurement points are replaced using linear interpolation through the neighboring artifacts-free data. The first reference point for linear interpolation is chosen to be the one right before the artifact. The second reference point is then defined during sequential scanning through the data points within 2 sec span after the artifact. This reference point is chosen as the closest one to the artifact that satisfies one of the additional conditions: (1) difference of the mean sphere between the two reference points should be less than 0.50 D; (2) the difference in the pupil diameter between the two reference points should be less than 1 mm; (3) the difference between the average pupil diameter (throughout the whole measurements set) and the second reference point should be less than 1 mm. If within the two seconds span there are no points satisfying any of the additional conditions, the seconds reference point is set to be that which is two seconds away from the artifact.

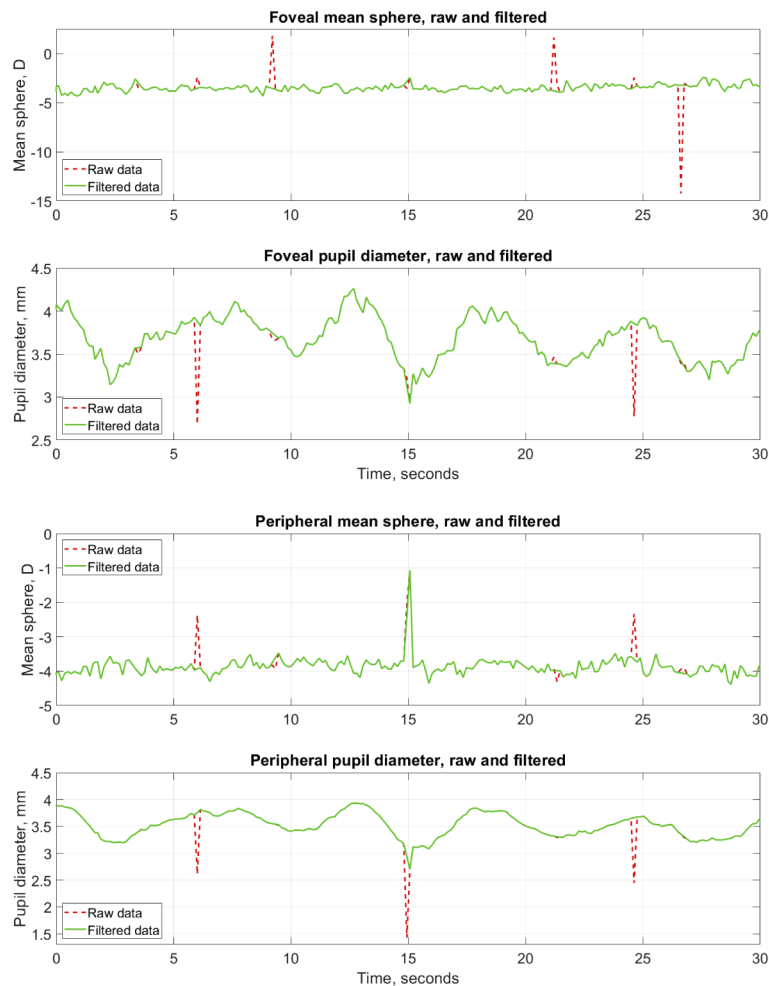


Fig. 2. An example of mean sphere and pupil diameter dynamics for fovea and 20° of the nasal visual field before and after implementation of the filtering algorithm. Dashed red line shows raw data and solid green line shows the data after filtering. The data are from measurements on Subject 2 (spherical equivalent $-2.75/-0.25 \times 175$).

After the post-processing, raw and filtered data for mean sphere and pupil diameter are manually examined. This allows to identify data sets with too many artifacts, that could not be processed correctly.

The efficacy of the proposed post-processing is demonstrated in Fig. 2 with an example of measured data before and after the processing. The 'raw data' and 'filtered data' curves clearly illustrate that the artifacts are removed while data of interest is intact.

3. Proof-of-concept measurements

The performance of the dual-angle open field wavefront sensor was assessed in two ways: using an artificial eye model, and collecting central and peripheral (20° nasal VF) wavefront data for three subjects. In both experiments, the wavefront was reconstructed up to the 6th order of Zernike polynomials. First, a hypermetropic eye model was sequentially measured on-axis by the two channels separately during 15 sec; the measurements were repeated five times. Average Zernike coefficients for these five measurements are given in Table 1 (Appendix 2). The average mean sphere values were $+4.44 \pm 0.17$ D and $+4.63 \pm 0.09$ D for Channel 1 and Channel 2 respectively. These values demonstrate a good inter-channel and intra-channel repeatability. The standard deviation of individual Zernike coefficients during each measurement set did not exceed $0.003 \mu\text{m}$ (4 mm pupil diameter) for individual coefficients.

Second, the real-time wavefront data was acquired from the right eye of three volunteers: one emmetropic (28 years old, Spherical Equivalent (SE) $+0.25/-0.25 \times 165$) and two myopic (30 years old, SE $-2.75/-0.25 \times 175$; 41 years old, SE $-1.75/-0.50 \times 140$). The data was acquired during three 30-sec sets for each subject. To avoid distractions, the subjects were in a dark room, fixating on a well-illuminated (photopic conditions) Maltese cross, located at 3.22 m (0.31 D of accommodation demand). The Zernike coefficients, as well as the refractive errors, were then calculated as the average over all of the measured data for each subject. The Zernike coefficients of all subjects are presented in Table 2 (Appendix 2). The measured aberrations agree with subjective refraction and earlier foveal measurements in other instruments (see Table 3, Appendix 2). The differences between foveal and peripheral aberrations are in accordance to previous publications on the population average ocular aberrations [48–53]. An example of the variation in central and peripheral Zernike coefficients for the emmetropic subject is given in Fig. 3.

In order to illustrate the potential usage of the proposed system with accommodation, two additional proof-of-concept experiments were conducted on the emmetropic subject. These experiments were (1) real-time wavefront measurements during three 30-sec sessions of accommodation to a 4.00 D target, and (2) real-time wavefront measurements during three 60-sec sessions with accommodation demand step-changes between 0.31 D and 4.00 D. Here, the wavefront was also reconstructed up to the 6th order of Zernike polynomials. All measurements were performed in a dark room (to avoid distractions) with well illuminated target (photopic conditions). For the far-away viewing, the fixation target was a Maltese cross. For the near-viewing, the target was a black-and-white picture with fine details, subtending 1.5° in diameter. In the experiment with the accommodation demand step-changes, both far and near targets were visible at the same time, and the subject was altering his fixation between the targets in 15-sec intervals. Results of the first experiment, together with the reference data for a relaxed eye, are given in Table 4 (Appendix 2). Results of the second experiment are demonstrated in Fig. 4. Here, foveal and peripheral mean sphere dynamics as well as RPR behavior during accommodation demand step-changes are shown. The foveal mean sphere curve clearly depicts the change in accommodation state of the eye every 15 sec of the experiment. Analysis of the RPR curve, however, does require some caution. Even though relatively small, the synchronization error (on average, 65 msec) gives rise to some artifacts at the time points of transition between the accommodation states (for example, the peaks at 15 and 30 seconds).

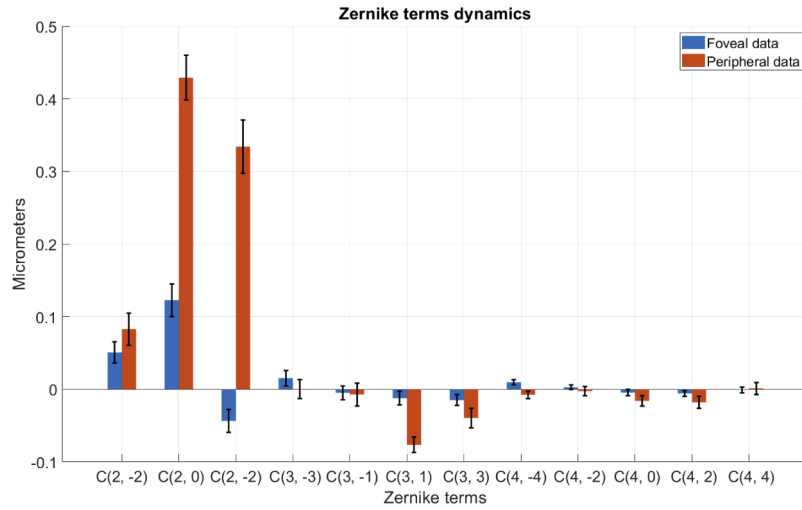


Fig. 3. An example of the dynamic wavefront measurements from the dual-angle open field wavefront sensor for fovea and 20° nasal visual field. The dynamics are described as the standard deviations of Zernike coefficients during one set of measurements (30 sec). The Zernike coefficients are given for 3 mm pupil diameter at $\lambda = 550$ nm. The subject was fixating at a far-away target (0.31 D of accommodation demand). The data is given for Subject 1 (spherical equivalent +0.25/-0.25 x 165)

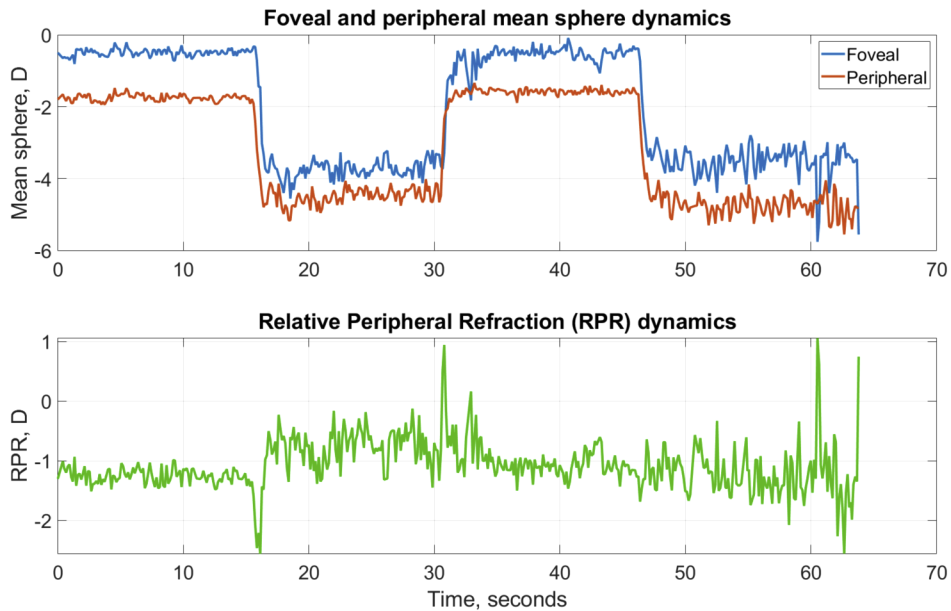


Fig. 4. Data from the dual-angle wavefront sensor for the accommodation demand step-change between 0.31 D and 4.00 D. Top: mean sphere dynamics for the fovea and 20° of the nasal visual field. Bottom: relative peripheral refraction for the 20° of the nasal visual field. The data is given for Subject 1 (spherical equivalent +0.25/-0.25 x 165).

4. Discussion

In the past years, several devices for multi-angle aberrations measurements have been developed. All of these devices are based on scanning of the VF. Most of them are state-of-the-art and are not available as commercial products. Taberner and Shaeffel [37] have presented an open-field scanning photoretinoscope, measuring refraction in $\pm 45^\circ$ of the horizontal VF in 4 sec. Jaeken et al. [54] introduced a fast scanning open field wavefront sensor, measuring $\pm 40^\circ$ of the horizontal VF in 1.8 sec. The BHVI-EyeMapper, described by Fedtke et al. [55], scans $\pm 50^\circ$ of the horizontal VF in 10° increments in less than half a second. This device, however, can measure only relaxed accommodation state due to the absence of fixation target. Finally, Wei and Thibos [56] developed a setup, taking 7 sec to measure 37 discrete locations in the central 30° of the VF (both horizontal and vertical). Of all the mentioned setups, only two [37,54] have an open field of view providing natural viewing conditions.

The dual-angle open field wavefront sensor presented here uses two wavefront sensors instead of VF scanning. Using one sensor for each eccentricity provides temporal resolution at least 10 times better compared to the scanning devices. The price for this speed is drastically decreased angular resolution: only two VF angles. The separation between these angles is further limited to the interval 15° - 30° .

High temporal resolution of the novel device enables the characterization of foveal and peripheral accommodation microfluctuations. The microfluctuations are small variations in the optical power of the eye caused by the dynamics of the crystalline lens shape. Previous work on accommodation microfluctuations concluded that they are mainly occurring at temporal frequencies below 2.5 Hz [38]. Therefore, according to the Nyquist sampling theorem, a minimal required frame rate to register the microfluctuations is 5 Hz. The dual-angle wavefront sensor operates at 7.5 ± 0.5 Hz, which is about 1.5 times higher than that threshold.

5. Summary

In this manuscript we propose a design of a dual-angle open field wavefront sensor. This wavefront sensor allows acquisition of simultaneous foveal and peripheral real-time wavefront data from a fixed eccentricity angle (can be chosen in the range of 15° - 30°) at 7.5 ± 0.5 Hz. Such a device enables the analysis of both average and dynamic parameters of the optical system of the human eye. The open field of view in the setup allows a broad spectrum of possible visual tasks as well as experiments in close-to-real-life conditions. The proposed device has many possible applications in myopia research requiring the usage of either static or dynamic accommodation demand.

Appendix 1

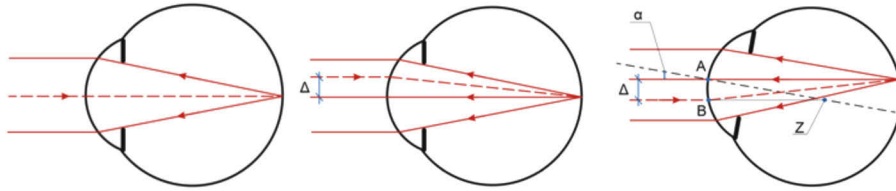


Fig. 5. Sources of the spotfield image decentration on the Hartmann-Shack wavefront sensor. Dashed lines show the reference light coming into the eye, and solid lines show the back-scattered light, captured by the wavefront sensor. *Left:* an ideal case when the subject is placed so that the exit pupil of the eye is centered with the wavefront sensor. The line of sight of the eye coincides with the optical axis of the wavefront sensor. In this case the spotfield image is perfectly centered on the wavefront sensor. *Middle:* the eye of the subject is laterally decentrated by Δ with respect to the optical axis of the wavefront sensor. The corresponding decentration of the spotfield image will be $\Delta \cdot M$, where M is the magnification between the exit pupil of the subject and the lenslet array of the wavefront sensor. *Right:* the eye of the subject is rotated by the angle α without lateral decentration. In this case the displacement of the spotfield image can be found from the triangle ABZ : $M \cdot \Delta = M \cdot AZ \cdot \tan(\alpha)$, where AZ — distance from the cornea to the centre of rotation of the eye, and α — rotation angle.

Appendix 2

Table 1. Repeatability of the on-axis measurements on a hypermetropic artificial eye model. The measurements were repeated 5 times; for each repetition the average Zernike coefficients were calculated. The table represents mean \pm standard deviation between these 5 sets of averaged Zernike coefficients. The coefficients are given for 4 mm pupil diameter at $\lambda = 550$ nm.

Zernike term	Channel 1	Channel 2
C(2; -2)	+0.024 \pm 0.010	+0.051 \pm 0.010
C(2; 0)	-2.875 \pm 0.024	-2.92 \pm 0.029
C(2; 2)	-0.004 \pm 0.004	-0.006 \pm 0.014
C(3; -3)	+0.012 \pm 0.025	+0.002 \pm 0.008
C(3; -1)	-0.048 \pm 0.019	+0.037 \pm 0.009
C(3; 1)	-0.003 \pm 0.004	+0.041 \pm 0.010
C(3; 3)	+0.001 \pm 0.010	+0.003 \pm 0.006
C(4; -4)	-0.002 \pm 0.011	0.000 \pm 0.009
C(4; -2)	+0.010 \pm 0.008	+0.003 \pm 0.005
C(4; 0)	-0.024 \pm 0.013	-0.015 \pm 0.007
C(4; 2)	+0.009 \pm 0.027	-0.015 \pm 0.005
C(4; 4)	-0.001 \pm 0.020	+0.006 \pm 0.004

Table 2. Average Zernike coefficients for fovea and 20° of the nasal visual field for 0.31 D accommodation demand. Subject 1: 28 years old, spherical equivalent +0.25/-0.25 x 165; Subject 2: 30 years old, spherical equivalent -2.75/-0.25 x 175; Subject 3: 41 years old, spherical equivalent -1.75/-0.50 x 140). Zernike coefficients are given for a 3 mm pupil diameter at $\lambda = 550$ nm.

Zernike terms	Foveal			Peripheral		
	Subject 1	Subject 2	Subject 3	Subject 1	Subject 2	Subject 3
C(2; -2)	+0.048	+0.053	+0.152	+0.085	+0.006	-0.017
C(2; 0)	+0.111	+1.180	+0.723	+0.425	+1.343	+0.601
C(2; 2)	-0.046	-0.073	+0.005	+0.344	+0.046	+0.258
C(3; -3)	+0.012	-0.020	-0.012	+0.010	+0.004	-0.003
C(3; -1)	0.000	+0.031	-0.030	-0.002	+0.032	+0.006
C(3; 1)	-0.009	+0.002	-0.029	-0.084	-0.025	-0.125
C(3; 3)	+0.009	0.000	+0.017	-0.041	-0.010	+0.008
C(4; -4)	+0.010	+0.003	0.01	-0.008	0.000	-0.008
C(4; -2)	+0.005	+0.009	+0.002	0.000	+0.011	+0.012
C(4; 0)	0.000	+0.014	+0.028	-0.014	+0.012	+0.026
C(4; 2)	-0.007	-0.005	+0.003	-0.018	+0.003	0.000
C(4; 4)	+0.003	-0.005	0.000	-0.001	+0.009	+0.005

Table 3. Cross-validation of the foveal measurements from the dual-angle wavefront sensor. Subject 1: 28 years old, spherical equivalent +0.25/-0.25 x 165; Subject 2: 30 years old, spherical equivalent -2.75/-0.25 x 175; Subject 3: 41 years old, spherical equivalent -1.75/-0.50 x 140). Foveal Zernike coefficients are given for 3 mm pupil diameter at $\lambda = 550$ nm.

Measurements method	Mean sphere, D		
	Subject 1	Subject 2	Subject 3
Subjective cycloplegic refraction	+0.13 D	-2.83 D	-2.00 D
Zeiss iProfiler (target at infinity)	-0.58 D	-3.34 D	No data
PlusOptix PowerRef 2 (target at 3.5 m)	+0.25 D	No data	No data
Dual-angle wavefront sensor (target at 3.22 m)	-0.33 D	-3.48 D	-1.89 D

Zernike terms	Subject 1, fovea		Subject 2, fovea	
	Dual angle wavefront sensor	Zeiss iProfiler	Dual angle wavefront sensor	Zeiss iProfiler
C(2; -2)	+0.048	+0.054	+0.053	+0.049
C(2; 0)	+0.111	+0.186	+1.180	+1.133
C(2; 2)	-0.046	-0.112	-0.073	-0.089
C(3; -3)	+0.012	-0.015	-0.020	-0.022
C(3; -1)	0.000	-0.005	+0.031	+0.012
C(3; 1)	-0.009	+0.018	+0.002	+0.010
C(3; 3)	+0.009	-0.006	0.000	0.000
C(4; -4)	+0.010	+0.005	+0.003	+0.005
C(4; -2)	+0.005	+0.007	+0.009	+0.002
C(4; 0)	0.000	+0.001	+0.014	+0.013
C(4; 2)	-0.007	-0.004	-0.005	-0.004
C(4; 4)	+0.003	+0.006	-0.005	-0.002

Table 4. Foveal and peripheral (20° nasal visual field) Zernike coefficients dynamics for an accommodating eye of Subject 1 (28 years, spherical equivalent +0.25/-0.25 x 165). Zernike coefficients are given for a 2.5 mm pupil diameter at $\lambda = 550$ nm. The values for 0.31 D of accommodation demand are calculated using data from Table 3.

Parameter	Target vergence: -0.31 D		Target vergence: -4.00 D	
	Fovea	20° nasal visual field	Fovea	20° nasal visual field
M	-0.33 D	-1.49 D	-3.46 D	-4.66 D
J0	+0.04 D	-1.09 D	+0.20 D	-0.87 D
J45	-0.06 D	-0.22 D	+0.16 D	+0.06 D
	Accommodation microfluctuations magnitude ^a : ± 0.15 D		Accommodation microfluctuations magnitude: ± 0.34 D	
Zernike term				
C(2; -2)	+0.029	+0.059	+0.003	+0.002
C(2; 0)	+0.077	+0.307	+0.800	+1.058
C(2; 2)	-0.026	+0.254	-0.053	+0.203
C(3; -3)	+0.008	+0.007	+0.001	+0.013
C(3; -1)	-0.001	-0.002	-0.001	-0.014
C(3; 1)	-0.006	-0.054	-0.002	-0.056
C(3; 3)	-0.005	-0.024	-0.019	-0.016
C(4; -4)	+0.005	-0.004	-0.006	-0.007
C(4; -2)	+0.002	0.000	+0.011	+0.007
C(4; 0)	0.2000	-0.007	+0.004	-0.001
C(4; 2)	-0.004	-0.011	0.000	-0.003
C(4; 4)	+0.001	0.000	+0.013	-0.002

^aAccommodation microfluctuations magnitude is assessed as \pm one standard deviation of the foveal mean sphere during one set of measurements. The average through 3 sets is thus the average of these standard deviations.

Funding

H2020 Marie Skłodowska-Curie Actions (675137).

Acknowledgements

The authors would like to gratefully acknowledge Associate Professor Peter Unsbo for all his useful insights during the design process.

The authors also would like to thank Frida Nero and the rest of the Thorlabs Sweden technical support team for their help during the device development process.

Disclosures

The authors declare no conflicts of interest.

References

1. J. M. Wood and R. Troutbeck, "Effect of restriction of the binocular visual field on driving performance," *Ophthalmic Physiol. Opt.* **12**(3), 291–298 (1992).
2. M. A. Wetton, M. S. Horswill, C. Hatherly, J. M. Wood, N. A. Pachana, and K. J. Anstey, "The development and validation of two complementary measures of drivers' hazard perception ability," *Accid. Analysis & Prev.* **42**(4), 1232–1239 (2010).
3. C. Owsley and G. McGwin Jr, "Vision impairment and driving," *Surv. Ophthalmol.* **43**(6), 535–550 (1999).
4. C. M. Patino, R. McKean-Cowdin, S. P. Azen, J. C. Allison, F. Choudhury, R. Varma, and L. A. L. E. S. Group, "Central and peripheral visual impairment and the risk of falls and falls with injury," *Ophthalmology* **117**(2), 199–206.e1 (2010).

5. A. Berencsi, M. Ishihara, and K. Imanaka, "The functional role of central and peripheral vision in the control of posture," *Hum. Mov. Sci.* **24**(5-6), 689–709 (2005).
6. E. W. Wiecek, L. R. Pasquale, J. Fiser, S. Dakin, and P. J. Bex, "Effects of peripheral visual field loss on eye movements during visual search," *Front. Psychol.* **3**, 472 (2012).
7. B. A. Holden, S. P. Mariotti, I. Kocur, S. Resnikoff, H. Mingguang, K. Naidoo, and M. Jong, "The impact of myopia and high myopia. Report of the Joint World Health Organization–Brien Holden Vision Institute Global Scientific Meeting on Myopia," (2015).
8. G. Smith, M. Millodot, and N. McBrien, "The effect of accommodation on oblique astigmatism and field curvature of the human eye," *Clin. Exp. Optom.* **71**(4), 119–125 (1988).
9. T. W. Walker and D. O. Mutti, "The effect of accommodation on ocular shape," *Optom. Vis. Sci.* **79**(7), 424–430 (2002).
10. L. Lundström, A. Mira-Agudelo, and P. Artal, "Peripheral optical errors and their change with accommodation differ between emmetropic and myopic eyes," *J. Vis.* **9**(6), 17 (2009).
11. A. Mathur, D. A. Atchison, and W. N. Charman, "Effect of accommodation on peripheral ocular aberrations," *J. Vis.* **9**(12), 20 (2009).
12. A. Whatham, F. Zimmermann, A. Martinez, S. Delgado, P. L. de la Jara, P. Sankaridurg, and A. Ho, "Influence of accommodation on off-axis refractive errors in myopic eyes," *J. Vis.* **9**(3), 14 (2009).
13. B. Holden, P. Sankaridurg, E. Smith, T. Aller, M. Jong, and M. He, "Myopia, an underrated global challenge to vision: where the current data takes us on myopia control," *Eye* **28**(2), 142–146 (2014).
14. P. K. Verkicharla, K. Ohno-Matsui, and S. M. Saw, "Current and predicted demographics of high myopia and an update of its associated pathological changes," *Ophthalmic Physiol. Opt.* **35**(5), 465–475 (2015).
15. K. M. Williams, G. Bertelsen, P. Cumberland, C. Wolfram, V. J. M. Verhoeven, E. Anastasopoulos, G. H. S. Buitendijk, A. Cougnard-Grégoire, C. Creuzot-Garcher, M. G. Erke, R. Hogg, R. Höhn, P. Hysi, A. P. Khawaja, J.-F. Korobelnik, J. Ried, J. R. Vingerling, A. Bron, J.-F. Dartigues, A. Fletcher, A. Hofman, R. W. A. M. Kuijpers, R. N. Luben, K. Oxele, F. Topouzis, T. von Hanno, A. Mirshahi, P. J. Foster, C. M. van Duijn, N. Pfeiffer, C. Delcourt, C. C. W. Klaver, J. Rahi, C. J. Hammond, and E. E. E. Consortium, "Increasing prevalence of myopia in Europe and the impact of education," *Ophthalmology* **122**(7), 1489–1497 (2015).
16. J. Wallman and J. Winawer, "Homeostasis of eye growth and the question of myopia," *Neuron* **43**(4), 447–468 (2004).
17. E. Goldschmidt and N. Jacobsen, "Genetic and environmental effects on myopia development and progression," *Eye* **28**(2), 126–133 (2014).
18. D. I. Flitcroft, "The complex interactions of retinal, optical and environmental factors in myopia aetiology," *Prog. Retinal Eye Res.* **31**(6), 622–660 (2012).
19. H.-M. Huang, D. S.-T. Chang, and P.-C. Wu, "The association between near work activities and myopia in children—a systematic review and meta-analysis," *PLoS One* **10**(10), e0140419 (2015).
20. L. Deng and Y. Pang, "Effect of outdoor activities in myopia control: meta-analysis of clinical studies," *Optom. Vis. Sci.* **96**(4), 276–282 (2019).
21. P.-C. Huang, Y.-C. Hsiao, C.-Y. Tsai, D.-C. Tsai, C.-W. Chen, C.-C. Hsu, S.-C. Huang, M.-H. Lin, and Y.-M. Liou, "Protective behaviours of near work and time outdoors in myopia prevalence and progression in myopic children: a 2-year prospective population study," *Br. J. Ophthalmol.* (2019).
22. G. Lingham, D. A. Mackey, R. Lucas, and S. Yazar, "How does spending time outdoors protect against myopia? A review," *Br. J. Ophthalmol.* **104**(5), 593–599 (2020).
23. S. A. McFadden, M. H. Howlett, and J. R. Mertz, "Retinoic acid signals the direction of ocular elongation in the guinea pig eye," *Vision Res.* **44**(7), 643–653 (2004).
24. L.-F. Hung, M. L. J. Crawford, and E. L. Smith, "Spectacle lenses alter eye growth and the refractive status of young monkeys," *Nat. Med.* **1**(8), 761–765 (1995).
25. A. R. Whatham and S. J. Judge, "Compensatory changes in eye growth and refraction induced by daily wear of soft contact lenses in young marmosets," *Vision Res.* **41**(3), 267–273 (2001).
26. E. L. Smith, C.-s. Kee, R. Ramamirtham, Y. Qiao-Grider, and L.-F. Hung, "Peripheral vision can influence eye growth and refractive development in infant monkeys," *Invest. Ophthalmol. Visual Sci.* **46**(11), 3965–3972 (2005).
27. A. Benavente-Pérez, A. Nour, and D. Troilo, "Axial eye growth and refractive error development can be modified by exposing the peripheral retina to relative myopic or hyperopic defocus," *Invest. Ophthalmol. Visual Sci.* **55**(10), 6765–6773 (2014).
28. F. Schaeffel, A. Glasser, and H. C. Howland, "Accommodation, refractive error and eye growth in chickens," *Vision Res.* **28**(5), 639–657 (1988).
29. E. L. Irving, J. G. Sivak, and M. G. Callender, "Refractive plasticity of the developing chick eye: a summary and update," *Ophthalmic Physiol. Opt.* **35**(6), 600–606 (2015).
30. E. L. Smith III, M. C. W. Campbell, and E. Irving, "Does peripheral retinal input explain the promising myopia control effects of corneal reshaping therapy (CRT or ortho-K) & multifocal soft contact lenses?" *Ophthalmic Physiol. Opt.* **33**(3), 379–384 (2013).
31. J. Huang, D. Wen, Q. Wang, C. McAlinden, I. Flitcroft, H. Chen, S. M. Saw, H. Chen, F. Bao, Y. Zhao, L. Hu, X. Li, R. Gao, W. Lu, Y. Du, Z. Jinag, A. Yu, H. Lian, Q. Jiang, Y. Yu, and J. Qu, "Efficacy comparison of 16 interventions for myopia control in children: a network meta-analysis," *Ophthalmology* **123**(4), 697–708 (2016).

32. C. S. Y. Lam, W. C. Tang, D. Y.-y. Tse, R. P. K. Lee, R. K. M. Chun, K. Hasegawa, H. Qi, T. Hatanaka, and C. H. To, "Defocus Incorporated Multiple Segments (DIMS) spectacle lenses slow myopia progression: a 2-year randomised clinical trial," *Br. J. Ophthalmol.* **104**(3), 363–368 (2020).
33. A. Mathur and D. A. Atchison, "Effect of orthokeratology on peripheral aberrations of the eye," *Optom. Vis. Sci.* **86**(5), E476–E484 (2009).
34. J. M. González-Méijome, M. A. Faria-Ribeiro, D. P. Lopes-Ferreira, P. Fernandes, G. Carracedo, and A. Queiros, "Changes in peripheral refractive profile after orthokeratology for different degrees of myopia," *Curr. Eye Res.* **41**(2), 199–207 (2016).
35. R. Calver, H. Radhakrishnan, E. Osobeni, and D. O'Leary, "Peripheral refraction for distance and near vision in emmetropes and myopes," *Ophthalmic Physiol. Opt.* **27**(6), 584–593 (2007).
36. L. N. Davies and E. A. H. Mallen, "Influence of accommodation and refractive status on the peripheral refractive profile," *Br. J. Ophthalmol.* **93**(9), 1186–1190 (2009).
37. J. Taberner and F. Schaeffel, "Fast scanning photoretinoscope for measuring peripheral refraction as a function of accommodation," *J. Opt. Soc. Am. A* **26**(10), 2206–2210 (2009).
38. W. N. Charman and G. Heron, "Microfluctuations in accommodation: an update on their characteristics and possible role," *Ophthalmic Physiol. Opt.* **35**(5), 476–499 (2015).
39. D. Seidel, L. S. Gray, and G. Heron, "Retinotopic accommodation responses in myopia," *Invest. Ophthalmol. Visual Sci.* **44**(3), 1035–1041 (2003).
40. M. Day, N. C. Strang, D. Seidel, L. S. Gray, and E. A. H. Mallen, "Refractive group differences in accommodation microfluctuations with changing accommodation stimulus," *Ophthalmic Physiol. Opt.* **26**(1), 88–96 (2006).
41. E. Harb, F. Thorn, and D. Troilo, "Characteristics of accommodative behavior during sustained reading in emmetropes and myopes," *Vision Res.* **46**(16), 2581–2592 (2006).
42. T. Langaas, P. M. Riddell, E. Svarverud, A. E. Ystenaes, I. Langeeggen, and J. R. Bruenech, "Variability of the accommodation response in early onset myopia," *Optom. Vis. Sci.* **85**(1), 37–48 (2008).
43. V. Sreenivasan, E. L. Irving, and W. R. Bobier, "Effect of near adds on the variability of accommodative response in myopic children," *Ophthalmic Physiol. Opt.* **31**(2), 145–154 (2011).
44. *Artificiell optisk strålning* (2019), p. 30.
45. F. Delori, R. Webb, and D. Sliney, "Maximum permissible exposures for ocular safety (ansi 2000), with emphasis on ophthalmic devices," *J. Opt. Soc. Am. A* **24**(5), 1250–1265 (2007).
46. T. O. Salmon, R. W. West, W. Gasser, and T. Kenmore, "Measurement of refractive errors in young myopes using the COAS Shack-Hartmann aberrometer," *Optom. Vis. Sci.* **80**(1), 6–14 (2003).
47. L. N. Thibos, M. Ye, X. Zhang, and A. Bradley, "The chromatic eye: a new reduced-eye model of ocular chromatic aberration in humans," *Appl. Opt.* **31**(19), 3594–3600 (1992).
48. A. Mathur, D. A. Atchison, and W. N. Charman, "Myopia and peripheral ocular aberrations," *J. Vis.* **9**(10), 15 (2009).
49. L. Lundström, J. Gustafsson, and P. Unsbo, "Population distribution of wavefront aberrations in the peripheral human eye," *J. Opt. Soc. Am. A* **26**(10), 2192–2198 (2009).
50. K. Baskaran, P. Unsbo, and J. Gustafsson, "Influence of age on peripheral ocular aberrations," *Optom. Vis. Sci.* **88**(9), 1088–1098 (2011).
51. B. Jaeken and P. Artal, "Optical quality of emmetropic and myopic eyes in the periphery measured with high-angular resolution," *Invest. Ophthalmol. Visual Sci.* **53**(7), 3405–3413 (2012).
52. P. Artal, ed., *Handbook of Visual Optics*, vol. 1 (CRC Press, 2017).
53. D. Romashchenko, R. Rosén, and L. Lundström, "Peripheral refraction and higher order aberrations," *Clin. Exp. Optom.* **103**(1), 86–94 (2020).
54. B. Jaeken, L. Lundström, and P. Artal, "Fast scanning peripheral wave-front sensor for the human eye," *Opt. Express* **19**(8), 7903–7913 (2011).
55. C. Fedtke, K. Ehrmann, D. Falk, R. C. Bakaraju, and B. A. Holden, "The BHVI-EyeMapper: peripheral refraction and aberration profiles," *Optom. Vis. Sci.* **91**(10), 1199–1207 (2014).
56. X. Wei and L. Thibos, "Design and validation of a scanning Shack Hartmann aberrometer for measurements of the eye over a wide field of view," *Opt. Express* **18**(2), 1134–1143 (2010).